



Cite this: *Phys. Chem. Chem. Phys.*,  
2017, 19, 2217

# Size-dependent one-photon- and two-photon-pumped amplified spontaneous emission from organometal halide $\text{CH}_3\text{NH}_3\text{PbBr}_3$ perovskite cubic microcrystals

Zhen-Yu Zhang,<sup>a</sup> Hai-Yu Wang,<sup>\*a</sup> Yan-Xia Zhang,<sup>a</sup> Kai-Jiao Li,<sup>b</sup> Xue-Peng Zhan,<sup>a</sup> Bing-Rong Gao,<sup>a</sup> Qi-Dai Chen<sup>a</sup> and Hong-Bo Sun<sup>\*a</sup>

In the past few years, organometal halide light-emitting perovskite thin films and colloidal nanocrystals (NCs) have attracted significant research interest in the field of highly purified illuminating applications. However, knowledge of photoluminescence (PL) characteristics, such as amplified spontaneous emission (ASE) of larger-sized perovskite crystals, is still relatively scarce. Here, we presented room-temperature size-dependent spontaneous emission (SE) and ASE of the organometal halide  $\text{CH}_3\text{NH}_3\text{PbBr}_3$  perovskite cubic microcrystals pumped through one-photon-(1P) and two-photon-(2P) excitation paradigms. The results showed that the optical properties of SE and ASE were sensitively dependent on the sizes of perovskite microcrystals irrespective of whether 1P or 2P excitation was used. Moreover, by comparing the spectral results of 1P- and 2P-pumped experiments, 2P pumping was found to be an effective paradigm to reduce thresholds by one order of magnitude. Finally, we carried out fluences-dependent time-resolved fluorescence dynamics experiments to study the underlying effects of these scale-dependent SE and ASE. We found that the photoluminescence (PL) recombination rates sensitively became faster with increasing carriers' densities, and that the ASE pumped from larger-sized  $\text{CH}_3\text{NH}_3\text{PbBr}_3$  perovskite cubic microcrystals showed faster lifetimes. This work shows that micro-sized perovskite cubic crystals could be the ideal patterns of perovskite materials for realizing ASE applications in the future.

Received 3rd November 2016,  
Accepted 9th December 2016

DOI: 10.1039/c6cp07522c

www.rsc.org/pccp

## Introduction

As a promising class of optical material, the past few years have witnessed the amazing development of luminescence applications of organometal halide perovskite semiconductors with the form  $\text{CH}_3\text{NH}_3\text{PbX}_3$  ( $X = \text{I}, \text{Br}, \text{Cl}$ ). These semiconductors have remarkable characteristics: commercially available solution-processed engineering;<sup>1–3</sup> remarkably high photoluminescence quantum yields (PLQYs) (almost  $\geq 85\%$ );<sup>4,5</sup> broad luminescence windows covering the entire visible spectral range;<sup>5,6</sup> high-purity narrow-band emission with full width at half maximum (FWHM) at only  $\sim 20$  nm;<sup>7,8</sup> ideal physical properties for realizing semiconductor lasers and amplified spontaneous emission (ASE).<sup>3,4,9–11</sup> These excellent characteristics have been partially or completely demonstrated in many perovskite patterns, including perovskite thin films whose grains sizes are  $< 10$   $\mu\text{m}$ ,<sup>7,12</sup> 2–20 nm-sized colloidal

nanocrystals (NCs) with cubic shape,<sup>5,13</sup> and large-sized perovskite crystals whose sizes have exceeded dozens of micrometers.<sup>6,14</sup>

Published works on small-sized perovskite-grain thin films<sup>15,16</sup> have demonstrated that the perovskite defects are universally present at the lattice grain boundaries and gaps of individual crystals, thereby preventing perovskite-based light-emitting devices from having an optimal performance. Fortunately, the defects and trap states can be almost ignored in perovskite NCs and large-sized perovskite crystals for different reasons. In colloidal perovskite NCs, the trap-states can be effectively passivated by the appropriate surface chemical capping ligands (such as *n*-octylamine) during their synthesis.<sup>7</sup> Large-sized perovskite crystals also show low trap-state density due to their relatively smaller crystal surface and grain boundaries.<sup>17,18</sup> Hence, NCs and large-sized perovskite crystals have been considered to be the next excellent research patterns to realize semiconductor lasing or high-purity ASE.<sup>9,14</sup> For instance, the Sun group<sup>4</sup> achieved halogen-related lasing from all-inorganic colloidal perovskite NCs; the Kovalenko group<sup>19</sup> observed low-threshold ASE and lasing from cesium lead halide perovskite NCs; the Zhu group realized high-Q lasers from perovskite nanowire lasers;<sup>20</sup> the Xiong group observed high-Q whispering gallery mode

<sup>a</sup> State Key Laboratory on Integrated Optoelectronics, College of Electronic Science and Engineering, Jilin University, 2699 Qianjin Street, Changchun 130012, China. E-mail: haiyu\_wang@jlu.edu.cn, hbsun@jlu.edu.cn

<sup>b</sup> College of Physics, Jilin University, 2699 Qianjin Street, Changchun 130012, China

(WGM) lasers from micro-scaled polygon platelets<sup>21</sup> and nanowires.<sup>22</sup>

These above-mentioned ASE were all pumped with 400 nm lasers (one-photon (1P) pumping paradigm) and this type of luminescence belongs to conventional Stokes fluorescence. Recently, the frequency up-conversion 2P absorption effects<sup>23–25</sup> in other materials have also been confirmed in perovskite materials<sup>13,26–28</sup> and this phenomenon brings another ASE pumped style. As is widely known, the penetration depth of 1P-excited light (400 nm lasers) is very small (<300 nm) due to its strong light absorption coefficient.<sup>18,26</sup> However, frequency up-conversion light (such as 800 nm) can penetrate much deeper into the crystal, and many more internal perovskite lattices can be excited due to their much weaker absorption intensity. Hence, when the thickness of perovskite crystals is very small, such as for perovskite NCs (sizes: ~9 nm), as proposed by the Xiao group,<sup>13</sup> the integral perovskite NCs are all run through by 400 or 800 nm pumping lasers. Due to the low conversion efficiency of nonlinear 2P effects, the corresponding ASE thresholds are usually much higher than the 1P excitation paradigm. However, if the thickness of perovskite cubic crystals increases to dozens or even hundreds of microns, 2P pumping will show great advantages because deeper internal lattices can be excited and a sharply increased gain length is obtained because of its much stronger light-penetration intensity. This physical mechanism indicates that the ASE threshold of these large-sized perovskite cubic crystals will be greatly reduced with a 2P pumping paradigm.

In the present work, we observed scale-dependent 1P- and 2P-pumped ASE of organometal halide  $\text{CH}_3\text{NH}_3\text{PbBr}_3$  perovskite cubic microcrystals. Also, we assessed the time-resolved fluences-dependent photoluminescence (PL) dynamics of the emission from different-sized  $\text{CH}_3\text{NH}_3\text{PbBr}_3$  cubic crystals. It was found that the properties of SE and ASE were very sensitive to the sizes of perovskite micro-sized cubic crystals. That is, the PL positions gradually red-shifted with increasing perovskite crystals sizes, and the ASE pumped from larger-sized perovskite microcrystals possessed relatively lower thresholds. More interestingly, due to the much stronger light-penetration intensity of 800 nm lasers, results showed that the 2P-pumped ASE threshold was reduced by one order of magnitude compared with the 1P pumping paradigm. The PL dynamics curves described from time-resolved experiments revealed that the fluorescence recombination rates were highly sensitive to the carriers' density, and that larger-sized perovskite crystals showed higher-purity ASE with faster lifetimes.<sup>29</sup>

## Experimental section

$\text{CH}_3\text{NH}_3\text{PbBr}_3$  perovskite cubic crystals were prepared by spinning a sub-saturated precursor solution on a quartz plate, and then thermal annealing these films in a nitrogen-filled glove box at ~80 °C for ~10 min. The sub-saturated precursor solution was synthesized by dissolving equimolar MABr and  $\text{PbBr}_2$  (8 mmol) into *N,N*-dimethylformamide (2 ml) with a concentration of the

saturated solution of ~65.75%. In general, the scales of  $\text{CH}_3\text{NH}_3\text{PbBr}_3$  cubic microcrystals can be carefully designed. This is achieved by designing the thickness of precursor saturated solution films by adjusting the coater spinning-cast velocity and time. The  $\text{CH}_3\text{NH}_3\text{PbBr}_3$  cubic crystals will be nucleated and then gradually grow along with drying out of the precursor solution during the thermal annealing process.<sup>30</sup> To assess the crystallization process, we performed morphology and scattering peak characterization on  $\text{CH}_3\text{NH}_3\text{PbBr}_3$  cubic microcrystals. The top-view scanning electron microscopy (SEM) images of three different-sized  $\text{CH}_3\text{NH}_3\text{PbBr}_3$  perovskite cubic crystals are shown in Fig. 1a–c (scale bar = 500  $\mu\text{m}$ ). Fig. 1d–f plots sectional thickness and length information of  $\text{CH}_3\text{NH}_3\text{PbBr}_3$  crystals measured by confocal laser scanning microscopy (CLSM). The inset of Fig. 1d–f shows the top-view simulated images of  $\text{CH}_3\text{NH}_3\text{PbBr}_3$  cubic microcrystals. The scales of these inset images are 500  $\times$  500  $\mu\text{m}$ . A quick glimpse at these SEM and CLSM images show that the precursor solution films with spin-coating velocities of 0, 50 and 500 rpm lasted for 30 s were perfectly formed isolated micron-sized  $\text{CH}_3\text{NH}_3\text{PbBr}_3$  cubic crystals whose sizes could be easily read at ~400, ~200 and ~100  $\mu\text{m}$ , respectively. To further examine the crystallization properties of these  $\text{CH}_3\text{NH}_3\text{PbBr}_3$  cubic microcrystals, we also obtained perovskite lattice X-ray diffraction (XRD) patterns from a powder Rigaku X-ray diffractometer (Fig. 1g). The patterns showed a set of strong lattice diffraction peaks with  $2\theta$  angles at 14.1°, 29.2°, and 44.8° which can be assigned, respectively, to the (110), (220) and (330) planes of  $\text{CH}_3\text{NH}_3\text{PbBr}_3$  crystals.<sup>9,31</sup> These XRD patterns matched the perovskite cubic system and observing the other miscellaneous peaks in these XRD spectra was difficult. This is indicative of the complete reaction between the precursor materials  $\text{CH}_3\text{NH}_3\text{Br}$  and  $\text{PbBr}_2$  during annealing.

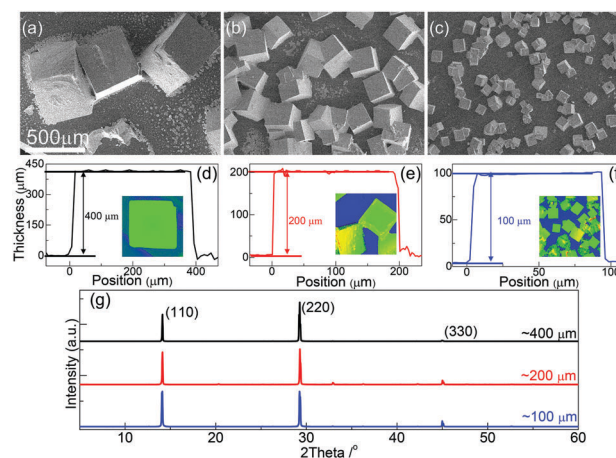


**Fig. 1** Top-view scanning electron microscopy (SEM) images of micron-sized  $\text{CH}_3\text{NH}_3\text{PbBr}_3$  perovskite cubic crystals with sizes at 400 (a), 200 (b) and 100  $\mu\text{m}$  (c), respectively. The scale bar is 500  $\mu\text{m}$ . (d), (e) and (f), respectively, show the cross-sectional thickness of 400, 200 and 100  $\mu\text{m}$ -sized  $\text{CH}_3\text{NH}_3\text{PbBr}_3$  perovskite cubic crystals by confocal laser scanning microscopy (CLSM). The inset shows the corresponding top-view simulated CLSM and the sizes are 500  $\times$  500  $\mu\text{m}$ . (g) Shows the X-ray diffraction (XRD) patterns of  $\text{CH}_3\text{NH}_3\text{PbBr}_3$  microcrystals of different sizes.

Optical band edges absorption spectra and PL spectra were observed by a Shimadzu UV-2550 spectrophotometer and a Hitachi F-4600 fluorescence spectrophotometer, respectively. During steady-state 1P- and 2P-pumped ASE measurements, a femtosecond 800 nm optical parametric amplifier (OPA) system was employed as the 2P pump source, and a 1P optical pump source of a 400 nm laser was generated by penetrating the output pulse (wavelength, 800 nm; repetition rate, 1 kHz; pulse width,  $\sim 100$  fs) through frequency doubling  $\beta$ -barium borate (BBO) crystals.

The laser beam was focused vertically by a convergent lens of dimension  $\sim 0.2 \times 0.2$  mm<sup>2</sup>. Pumped PL signals were collected vertically by a lens and then analyzed by a highly sensitive AvaSpec-2048 fiberoptic spectrometer.

Nanosecond time-resolved PL emission experiments were performed by a time-correlated single-photon counting (TCSPC) system under right-angle sample geometry. Briefly, a picosecond diode laser (EPL405; Edinburgh Instruments) outputted a wavelength of 405 nm at repetition rates of 2 MHz. The sample was excited by 405 nm and the fluorescence signals were selected by a monochromatic wavelength and amplified by a photomultiplier tube (Hamamatsu H5783p). Kinetics were recorded at a TCSPC board (SPC-130; Becker and Hickel). Time constant of the instrument response function was  $\sim 300$  ps. Picosecond time-resolved PL dynamics were measured by the femtosecond fluorescence up-conversion method. A femtosecond OPA (RGA, Spitfire; Spectra Physics) outputted 800 nm lasers with pulse energy of 1.5 mJ and pulse width of 100 fs. The 800 nm wavelength was split into two parts; the second harmonic (400 nm) of one beam was focused on the sample as excitation. The resultant fluorescence was collected and focused onto a 1 mm-thick BBO crystal with a cutting angle of 35°. The other part of the RGA output was sent to an optical delay line and served as the optical gate for up-conversion of fluorescence. The generated sum frequency signals were then collimated and focused into the entrance slit of a 300 mm monochromator. A UV-sensitive photomultiplier tube (1P28; Hamamatsu) was used to detect the signal. The electrical signal from the photomultiplier tube was summed by a digital oscilloscope. The probe wavelength was chosen at the peak of the ASE position. These lifetimes of the measured kinetic curves were then calculated by ASUFIT data analysis software. All measurements were performed at room temperature in air.

## Results and discussion

Before studying the pumped ASE, we first investigated the influence of the sizes, from dozens of nanometers to hundreds of micrometers, on the absorption and PL properties of CH<sub>3</sub>NH<sub>3</sub>PbBr<sub>3</sub> cubic crystals. Fig. 2a displays a series of optical absorption spectra of CH<sub>3</sub>NH<sub>3</sub>PbBr<sub>3</sub> cubic crystals with sizes at  $< 1$  (black),<sup>7</sup>  $\sim 100$  (red),  $\sim 200$  (blue) and  $\sim 400$   $\mu\text{m}$  (magenta) with the measured band-edge absorption (marked by dashed lines) being easily read at 520, 528, 536 and 555 nm, respectively. As direct-gap semiconductors, these perovskite emitters will show

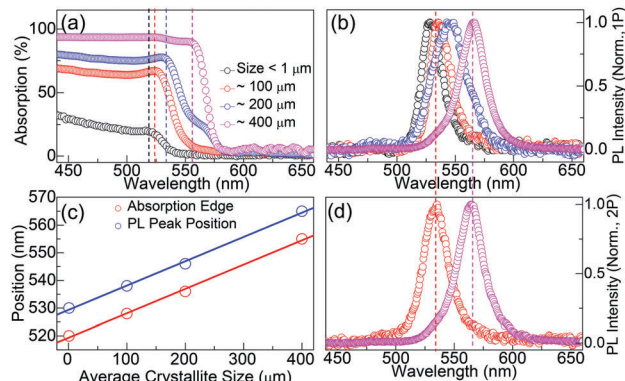


Fig. 2 (a) and (b), respectively, present the size-resolved UV-vis absorption and 1P-pumped photoluminescence (PL) spectra for perovskite cubic crystals of different sizes at  $< 1$  (black), 100 (red), 200 (blue) and 400  $\mu\text{m}$  (magenta). (c) Shows the spectral positions of the UV-vis absorption band edge and 1P-pumped SE peak positions as linear functions of crystallite sizes. (d) Gives the 2P-pumped of these two different CH<sub>3</sub>NH<sub>3</sub>PbBr<sub>3</sub> perovskite crystals with sizes of 100 (red) and 400  $\mu\text{m}$  (magenta), respectively.

narrow PL peaks near the band edge.<sup>7,17</sup> As presented in Fig. 2b, these crystals also exhibited narrow PL peaks, and the peaks near the band edge could be easily read at 529 (black), 536 (red), 546 (blue) and 565 nm (magenta), respectively. Similar to the study of the Petrozza group,<sup>20</sup> Fig. 2c reveals that the absorption shoulders and PL peak positions linearly shifted to longer wavelengths (lower energies) with increasing sizes of perovskite cubic crystals while keeping a constant Stokes shift at  $\sim 10$  nm. Based on our best knowledge, the red-shift of the exciton energy and band with increasing crystal size can be explained by the size-dependent evolution of the bulk- and surface-mechanism. That is, the bulk effect ( $\sim 560$  nm)<sup>17</sup> becomes more dominating with increasing sizes of perovskite crystals, and vice versa for the surface effect ( $\sim 520$  nm). Hence, the band gap red-shifted from 528 to 555 nm when the size increased from 100 to 400  $\mu\text{m}$ . Fig. 2d shows the intensity-normalized 2P-pumped PL spectra of CH<sub>3</sub>NH<sub>3</sub>PbBr<sub>3</sub> cubic crystals with sizes at 100 (red) and 400 (magenta)  $\mu\text{m}$ , respectively. Instructed by the marked dashed lines in Fig. 2b and d, it can be seen that the 2P-pumped PL peaks of 100 and 400  $\mu\text{m}$ -sized crystals can be read at 536 and 565 nm, respectively,<sup>7,17</sup> showing the same corresponding PL peaks compared with the 1P-pumped experiment. The PL shown in Fig. 2d confirmed the 2P absorption effect of perovskite materials, and this paves the way for visible lasing or ASE applications with an infrared 2P pumping paradigm.

To perform the 1P-pumped ASE experiments, a second-harmonic 400 nm femtosecond pulsed laser beam (pulse width:  $\sim 100$  fs) of an OPA was used to excite these CH<sub>3</sub>NH<sub>3</sub>PbBr<sub>3</sub> cubic crystals. These PL signals were collected by a vertical optical lens and then analyzed by a highly sensitive AvaSpec-2048 fiber optic spectrometer. Fig. 3a–c, respectively, illustrate the representative fluence-dependent PL spectra of 100, 200 and 400  $\mu\text{m}$ -sized CH<sub>3</sub>NH<sub>3</sub>PbBr<sub>3</sub> cubic crystals. Fig. 3d–f, respectively, plot the corresponding emission intensities and FWHM as functions of pumped fluences  $P_{\text{pump}}$ . Fig. 3a shows the fluences-resolved PL

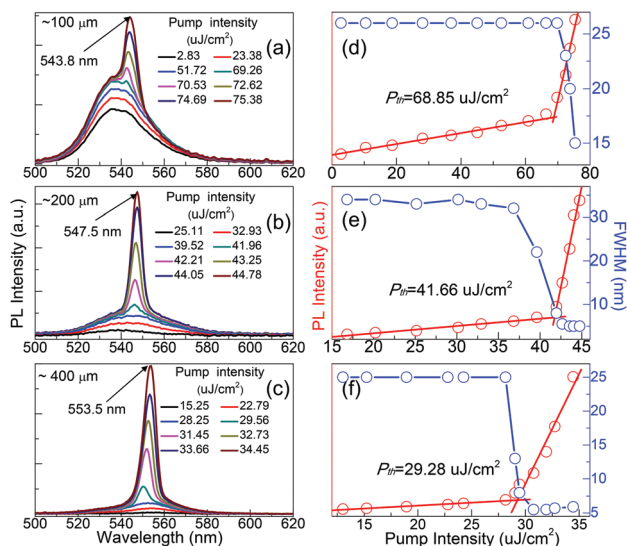


Fig. 3 Left panel: Fluences-resolved PL emission spectra of 100 (a), 200 (b) and 400 μm-sized (c)  $\text{CH}_3\text{NH}_3\text{PbBr}_3$  cubic crystals around the amplified spontaneous emission (ASE) thresholds. Right panel: The emission intensity and full width at half maximum (FWHM) of ASE pumped from 100 (d), 200 (e) and 400 μm-sized (f)  $\text{CH}_3\text{NH}_3\text{PbBr}_3$  microcrystals are plotted as a function of excitation intensity  $P_{\text{pump}}$ .

spectra pumped from  $\sim 100$  μm-sized  $\text{CH}_3\text{NH}_3\text{PbBr}_3$  cubic crystals. When  $P_{\text{pump}}$  was  $< 51.72$  μJ cm<sup>-2</sup>, all the emission spectra showed identical broad peaks centered at  $\sim 536$  nm with FWHM at 26 nm, and these peak intensities grew very slowly with increasing  $P_{\text{pump}}$ . That is, the PL emission was still dominated by the relatively broad intrinsic SE under relatively low excited intensities. When  $P_{\text{pump}} \geq 69.26$  μJ cm<sup>-2</sup>, a sharp emission peak at 543.8 nm emerged from broad SE spectra, whose peaks were longer than SE peaks. The spectrogram shows that the PL peaks at 543.8 nm started narrowing and that their intensity grew so fast that the intensity of the broad SE peaks of 536 nm remained almost identical when  $P_{\text{pump}}$  slightly increased from 69.26 to 75.38 μJ cm<sup>-2</sup>. Fig. 3d plots the integrated PL intensity (red circle) and the FWHM (blue circle) of 543.8 nm as functions of laser  $P_{\text{pump}}$  ranging from 2.83 to 75.38 μJ cm<sup>-2</sup>. The fitted relationships between PL intensity and  $P_{\text{pump}}$  were composed of two linear increasing behaviors. The low-sloped linear equation donates only the fluence-dependent SE process. The high-sloped linear equation mainly expresses the fluence-dependent ASE process accompanied by a slight SE process. By solving the node of the two linear equations, it could be seen that the ASE threshold of 100 μm-sized  $\text{CH}_3\text{NH}_3\text{PbBr}_3$  crystals showed  $P_{\text{th}}$  to be 68.85 μJ cm<sup>-2</sup>. In terms of spectra, ASE is a fluorescence line width-narrowing operation. As illustrated in Fig. 3d, the FWHM showed a constant value at 26 nm when  $P_{\text{pump}} < P_{\text{th}}$ , whereas the FWHM suddenly dropped from 26 to 15 nm at an amazing speed when  $P_{\text{pump}} \geq P_{\text{th}}$ . Under sufficient laser  $P_{\text{pump}}$  ( $> 75.38$  μJ cm<sup>-2</sup>), the FWHM of pure ASE should be 5–6 nm similar to Fig. 3e and f.

Fig. 3 shows that the ASE position and  $P_{\text{th}}$  value were very sensitive to the sizes of  $\text{CH}_3\text{NH}_3\text{PbBr}_3$  cubic crystals. The left part of Fig. 3 shows that the ASE peaks gradually red-shifted

from 543.8 to 547.5 and 553.5 nm when crystal scales increased from 100 to 200 and 400 μm. In general, the ASE or lasing modes are usually modulated by the cavity configurations. As illustrated by the Sargent group,<sup>32</sup> the optical modes of these perovskite cubic crystals can be still considered to be a combination of traditional lengthwise Fabry–Perot mode and the transverse WGM. These optical modes are very sensitive to the sizes of the crystals. The left part of Fig. 3 shows that the ASE peaks of 100 μm-sized and 200 μm-sized (543.8 and 547.5, respectively) were all longer than their SE peaks (536 nm and 546 nm, respectively), whereas the ASE peak of 400 μm-sized was much shorter (553.5 nm) than its SE peak (565 nm). That is, the ASE positions can be dominated by the size-dependent optical mode of these perovskite cubic crystals. The results in the right part of Fig. 3 show that the ASE threshold is also size-dependent: the  $P_{\text{th}}$  reduced from 68.85 μJ cm<sup>-2</sup> of 100 μm-sized crystals to 41.66 μJ cm<sup>-2</sup> of 200 μm-sized crystals and further reduced to 29.28 μJ cm<sup>-2</sup> of 400 μm-sized samples. Our samples had hundred micrometer-sizes, which are all much larger than the penetration depth of 400 nm lasers into the crystals. Hence, the reduced  $P_{\text{th}}$  in larger-sized crystals can be attributed only to its relative smaller surface states<sup>17,18</sup> due to its small ratio of surface area to volume. In our previous work,<sup>7</sup> it was found that the surface defect states trapped the photo-generated carriers and reduced the quantities of free charge carriers. That is, the larger-sized crystals possessed much more free carriers to realize ASE. Taking  $P_{\text{pump}} = 34.45$  μJ cm<sup>-2</sup>, for example, the 400 μm-sized samples possessed a sufficient number of carriers to realize population inversion and the resultant ASE. However, for 100 and 200 μm-sized crystals, the photo-induced free carriers' density was much lower than the critical intensity, and the resultant PL spectra were still dominated by broad SE due to the influences of surface defects states.

Fig. 4a is a schema showing the absorption and fluorescence of  $\text{CH}_3\text{NH}_3\text{PbBr}_3$  cubic crystals under 1P (left part) and 2P (right part) excitation, respectively. Compared with 1P excitation, though the energy of a pumping laser of 800 nm was far below the band gap of  $\text{CH}_3\text{NH}_3\text{PbBr}_3$  crystals, two 800 nm photons can also be simultaneously absorbed through the virtual states.<sup>13,23–28</sup> After going through the band-filling process,<sup>33</sup> the populated excited states carriers will radiate jumping from a conduction-band minimum to a valence-band maximum, emitting fluorescence photons with the same energy. Representative 2P-pumped fluences-resolved PL spectra of 100 and 400 μm-sized  $\text{CH}_3\text{NH}_3\text{PbBr}_3$  cubic crystals around the ASE  $P_{\text{th}}$  are illustrated in Fig. 4b and c, respectively. Similar to 1P-excitation shown in Fig. 3, taking a 100 μm-sized sample (in Fig. 3b), for example, when  $P_{\text{pump}}$  is  $< 4.5$  μJ cm<sup>-2</sup>, each emission spectrum showed a broad SE peak centered at  $\sim 535$  nm with FWHM at 26 nm and the SE peak intensities grew very slowly with increasing  $P_{\text{pump}}$ . When  $P_{\text{pump}} \geq 6.2$  μJ cm<sup>-2</sup>, a sharp emission peak at 543.8 nm emerged on the right side of a broad PL spectrum and the intensities of this narrowed 1P-pumped ASE grew so fast that the intensity of the broad SE remained almost identical when  $P_{\text{pump}}$  increased from 6.2 to 9.3 μJ cm<sup>-2</sup>. Compared with 1P-pumped fluence-dependent PL spectra, the 2P-pumped PL

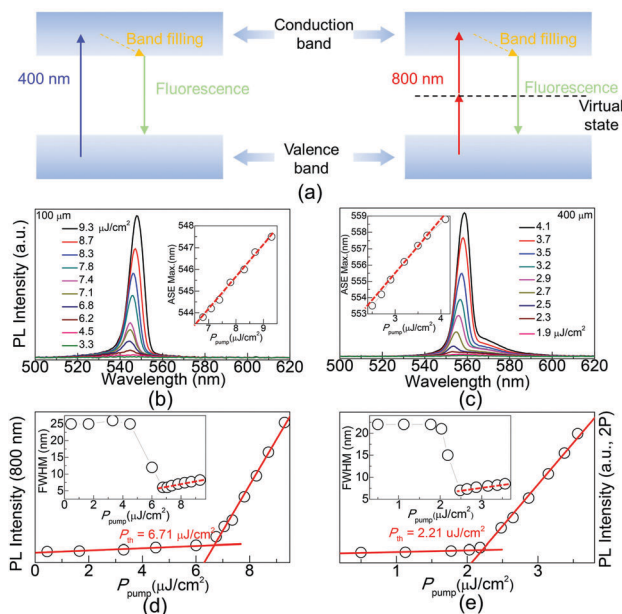


Fig. 4 (a) Illustrates the photophysical absorption and fluorescence processes under 1P- (left) and 2P-excitation (right). We achieved fluences-dependent 2P-pumped ASE from perovskite cubic crystals with different sizes at 100 (b) and 400  $\mu\text{m}$  (c), respectively. (d) and (e), respectively, plot emitted integral intensity and FWHM (insets) of ASE as functions of pump laser fluences for 100- (d) and 400  $\mu\text{m}$ -sized (e) perovskite cubic crystals.

signals showed two evident differences: fluences-dependent red-shift and broadened effects. The insets of Fig. 4b and c, respectively, give the linear-dependent relationships (marked by red dashed lines) between the positions of ASE maximum and  $P_{\text{pump}}$ : ASE peak linearly red-shifted with increased  $P_{\text{pump}}$ . Here, taking 100  $\mu\text{m}$ -sized crystals, for example (Fig. 3a and 4b), with increasing  $P_{\text{pump}}$  ( $>P_{\text{th}}$ ), the 2P-pumped ASE gradually linearly red-shifted from 543.8 to 547.5 nm (shown in the inset) whereas 1P-pumped ASE were almost fixed at 543.8 nm. Broadened spectra under higher  $P_{\text{pump}}$  have also been observed by the Kamat group, and they proposed that the broadening phenomenon is indicative of charge carrier accumulation and can be explained on the basis of a dynamic Burstein–Moss shift,<sup>33</sup> namely, the broadened intensity of ASE is sensitively related to carriers' densities. As mentioned above, the 2P 800 nm lasers can easily penetrate into the internal crystal and trigger many more internal charge carriers compared with 1P excitation. As a result, as shown in Fig. 4b and c, the 2P-pumped ASE broadening effect was much more evident than that of the 1P pumping paradigm. Fig. 4d and e plot integral 2P-pumped PL intensities as functions of laser  $P_{\text{pump}}$  and insets also show the relationships between the FWHM of fluorescence maximum and laser  $P_{\text{pump}}$ . Similar to 1P-excitation, the larger-sized  $\text{CH}_3\text{NH}_3\text{PbBr}_3$  perovskite cubic crystals also showed relatively lower ASE  $P_{\text{th}}$ : 6.71  $\mu\text{J cm}^{-2}$  for a 100  $\mu\text{m}$ -sized sample and 2.21  $\mu\text{J cm}^{-2}$  for a 400  $\mu\text{m}$ -sized sample. In general, due to the low conversion efficiency of nonlinear 2P effects, the corresponding ASE thresholds are usually much higher than the 1P excitation paradigm. As presented by Xiao<sup>13</sup> and Mohammed groups,<sup>26</sup> 400 and 800 nm both penetrated NCs and films, with the same line

gain length, with the ASE using 2P excitation being much higher than that of the 1P excitation paradigm. While this phenomenon will not happen in dozens of micrometer-sized crystals, according to the Beer–Lambert law, the 800 nm lasers can “punch” into the crystals with 30–60  $\mu\text{m}$ , indicating that the line gain length is nearly 100-times longer than that of 400 nm lasers. In addition, much more perfect internal perovskite lattices are excited by 800 nm lasers. In the present work, compared with 1P excitation, the 2P-pumped ASE  $P_{\text{th}}$  was reduced by nearly one order of magnitude. As illustrated in spectrograms, the  $P_{\text{th}}$  of 100  $\mu\text{m}$ -sized crystals was reduced from 68.85 to 6.71  $\mu\text{J cm}^{-2}$ , and the  $P_{\text{th}}$  of 400  $\mu\text{m}$ -sized crystals was reduced from 29.28 to 2.21  $\mu\text{J cm}^{-2}$ . In terms of spectra, the ASE is a fluorescence-narrowing operation. As illustrated in the insets, the FWHM shows a constant value at  $\sim 26$  nm when  $P_{\text{pump}} < P_{\text{th}}$  whereas, when  $P_{\text{pump}} \geq P_{\text{th}}$ , the FWHM suddenly dropped from 26 to 5–6 nm with amazing speed. The results show that the 1P-pumped ASE had constant FWHM value (insets of Fig. 4d and e) whereas 2P-pumped ASE was slightly linear (marked by red dashed lines) and broadened with increasing  $P_{\text{th}}$  due to a band-filling effect (induced by charge carrier accumulation) in perovskite materials.<sup>33</sup> For example, taking 400  $\mu\text{m}$ -sized crystals (Fig. 3f and 4e), with increasing  $P_{\text{pump}}$  ( $>P_{\text{th}}$ ), the FWHM of 1P-pumped ASE was nearly fixed at 5.3 nm, whereas the line-width of 2P-pumped ASE linearly increased from 5.3 to 8.3 nm, indicating a linear relationship between broadening ASE line-width with  $P_{\text{pump}}$ .

Now, we had completed the steady-state size-dependent 1P and 2P pumped ASE measurements. Deeper understanding of the SE and ASE would come from time-resolved PL dynamics experiments performed by a nanosecond time-resolved TCSPC and picosecond time-resolved fluorescence up-conversion system. Fig. 5a and b, respectively, plot the fluence-dependent PL decay kinetics of 100 and 400  $\mu\text{m}$ -sized  $\text{CH}_3\text{NH}_3\text{PbBr}_3$  crystals under low laser  $P_{\text{pump}}$  (2.5  $\text{nJ cm}^{-2}$ , red circles) and

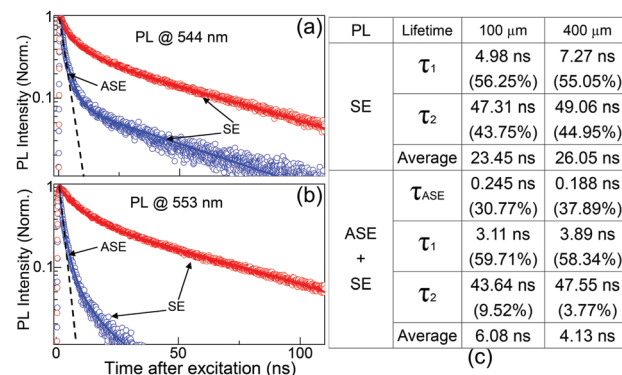


Fig. 5 Time-resolved nanosecond fluorescence dynamics performed by a time-correlated single-photon counting system for 100 (a) and 400  $\mu\text{m}$ -sized (b)  $\text{CH}_3\text{NH}_3\text{PbBr}_3$  cubic microcrystals. The dashed black lines indicate the ASE decay process. (c) Illustrates the fitted component dynamics and corresponding lifetimes of each kinetic curve. The fitted errors are  $\leq 2\%$ . The PL decay kinetics after photoexcitation with laser  $P_{\text{pump}} > P_{\text{th}}$  (blue) show a  $\sim 0.2$  ns ASE lifetime, one that is  $>100$ -times faster than that of SE decay kinetics with laser  $P_{\text{pump}} < P_{\text{th}}$  (red).

high laser  $P_{\text{pump}}$  ( $50 \text{ nJ cm}^{-2}$ , blue circles). The fitted results are plotted as lines and the ASE recombination processes are marked by black dashed lines. Fig. 4c shows the fitted component dynamics and corresponding ratios. All the fitted errors were  $\leq 2\%$ . Different from our previous PL dynamics experiments on small-grain thin films,<sup>7</sup> we estimated the PL decay (excited with low power lasers) of  $\text{CH}_3\text{NH}_3\text{PbBr}_3$  cubic microcrystals as two components: a shorter-lived component  $\tau_1$  (a few nanoseconds) and a slower decay  $\tau_2$  (tens of nanoseconds).<sup>17</sup> When excited with higher power lasers, another PL decay component – ASE kinetics  $\tau_{\text{ASE}}$  – emerged, showing much faster decay rates than that of SE. Here, we took  $400 \mu\text{m}$ -sized  $\text{CH}_3\text{NH}_3\text{PbBr}_3$  cubic microcrystals for quantitative analyses. The apparent SE lifetime was as long as  $\tau_{\text{Average}} = 26.05 \text{ ns}$  under low excitation intensity, with  $\tau_1 = 7.27 \text{ ns}$  (55.05%) and  $\tau_2 = 49.06 \text{ ns}$  (44.95%). However, the PL (SE and ASE) lifetime rapidly decreased to  $\tau_{\text{Average}} = 4.13 \text{ ns}$  under high excitation intensity due to an ASE process with  $\tau_{\text{ASE}} = 0.188 \text{ ns}$  (37.89%), along with  $\tau_1 = 3.89 \text{ ns}$  (58.34%) and  $\tau_2 = 47.55 \text{ ns}$  (3.77%). The ASE lifetime was  $>100$ -times faster than that of SE. Compared with the  $400 \mu\text{m}$ -sized sample, due to its relative higher threshold,  $100 \mu\text{m}$ -sized crystals showed a slower lifetime with  $\tau_{\text{ASE}} = 0.245 \text{ ns}$  and a lower ratio (30.77%) under the same excitation intensity.

We carried out further time-resolved femtosecond up-conversion measurement for SE and ASE of  $\text{CH}_3\text{NH}_3\text{PbBr}_3$  cubic emitters. Fig. 6a–c, respectively, show the spectrally integrated PL decay curves of  $100$ ,  $200$  and  $400 \mu\text{m}$ -sized  $\text{CH}_3\text{NH}_3\text{PbBr}_3$  cubic crystals, and the detected PL signals were modulated at  $543.8$ ,  $547.5$  and  $553.5 \text{ nm}$ . These integral kinetic traces were split into two parts, with the former build-up signal expressing the carriers' band-filling process and the latter decay signal being donated to the carriers' recombination process. In Fig. 6d, the fitted decay lifetime and corresponding proportion of each kinetics curves shown in Fig. 6a–c are reported. The fitted dynamic lifetimes' errors are all  $\leq 2\%$ . Under low laser  $P_{\text{pump}}$  ( $\leq 28 \mu\text{J cm}^{-2}$ ), analogs to TCSPC measurements, each measured (circles) PL decay trace was also fitted as the composition of (lines) rapid Auger recombination ( $\tau_1$ ) and free electron–hole recombination ( $\tau_2$ ). The Auger effect will be more evident while the recombination between free holes and electrons will be weakened with increasing charge carriers density. Taking  $400 \mu\text{m}$ -sized cubic crystals, for example, the ratio of  $\tau_1$  increased from 38.21% to 64.49%, whereas the ratio of  $\tau_2$  decreased from 61.79% to 35.51%, when  $P_{\text{pump}}$  increased from  $15$  to  $28 \mu\text{J cm}^{-2}$ . Under an identical laser  $P_{\text{pump}}$ , the weakened Auger effects can be attributed to the relatively lower carriers' density in larger-sized  $\text{CH}_3\text{NH}_3\text{PbBr}_3$  emitters whereas, for the recombination between free holes and electrons, the converse is true. For example, with  $P_{\text{pump}} = 15 \mu\text{J cm}^{-2}$ , the ratio of  $\tau_1$  fell from 65.96% to 38.21% and the ratios of  $\tau_2$  increased from 34.04% to 61.79%, when sizes increased from  $100$  to  $400 \mu\text{m}$ . Similar to our previous works,<sup>7,31</sup> the PL decay dynamics lifetimes showed strong fluence-dependence: the kinetic decay rates become faster with increasing carriers' density or  $P_{\text{pump}}$ . For example, in  $400 \mu\text{m}$ -sized perovskite crystals, when  $P_{\text{pump}}$  increased from  $15$  to  $28 \mu\text{J cm}^{-2}$ , the Auger recombination lifetimes decreased from  $46.27$  to  $29.54 \text{ ps}$ , the free electron–hole

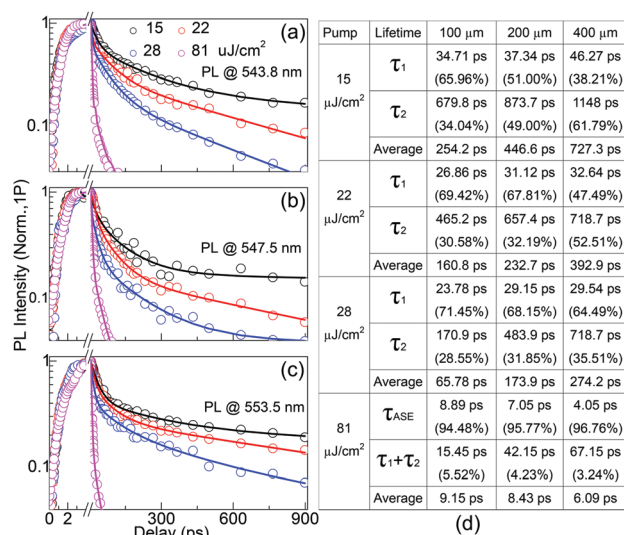


Fig. 6 Time-resolved picosecond fluorescence dynamics observed from femtosecond fluorescence up-conversion experiments for  $100$  (a),  $200$  (b) and  $400 \mu\text{m}$ -sized (c)  $\text{CH}_3\text{NH}_3\text{PbBr}_3$  cubic microcrystals, respectively. (d) Illustrates the fitted component dynamics and corresponding lifetimes of each kinetic curve. The fitted errors are  $\leq 2\%$ . When  $P_{\text{pump}} < P_{\text{th}}$ , the PL decay kinetics curves show strong fluences-dependent characteristics: the SE recombination rates gradually increase with increasing excitation intensity. When  $P_{\text{pump}} > P_{\text{th}}$ , the PL is almost dominated by the ASE, showing much faster lifetimes (a few picoseconds) compared with that of SE (hundreds of picoseconds).

recombination lifetimes decreased from  $1148$  to  $718.7 \text{ ps}$  and the average lifetimes fell from  $727.3$  to  $274.2 \text{ ps}$ . Under high laser  $P_{\text{pump}}$  ( $81 \mu\text{J cm}^{-2}$ , exceeding all the thresholds of  $\text{CH}_3\text{NH}_3\text{PbBr}_3$  emitters shown in Fig. 3), it was found that the ASE effect had a dominant role (illustrated by magenta circles and lines), resulting in amazingly faster PL decay dynamics in these spectrograms. We fitted these decay dynamics as a combination of ASE and SE processes. The  $P_{\text{pump}}$  far exceeded  $P_{\text{th}}$ , so the ASE process almost dominated the PL process. As illustrated in Fig. 6d, the ratios of ASE were 94.48%, 95.77% and 96.76% for  $100$ ,  $200$  and  $400 \mu\text{m}$ -sized emitters, respectively, and showed a slightly increasing trend with increasing crystal sizes. The fitted decay lifetimes of ASE were  $8.89$ ,  $7.05$  and  $4.05 \text{ ns}$  for  $100$ ,  $200$  and  $400 \mu\text{m}$ -sized emitters, respectively, showing a faster trend with increasing crystal sizes. Compared with the lifetime of SE under low  $P_{\text{pump}}$  ( $15 \mu\text{J cm}^{-2}$ ), the accelerated factors of ASE pumped from  $100$ ,  $200$  and  $400 \mu\text{m}$ -sized emitters were  $28.6$ ,  $63.3$  and  $179.6$ , respectively. In addition, the integral PL lifetimes were also greatly reduced when the dominated ASE process emerged. These time-resolved dynamics showed that the larger-sized  $\text{CH}_3\text{NH}_3\text{PbBr}_3$  cubic crystals exhibited highly purified and faster ASE due to their lower  $P_{\text{th}}$ . Finally, we examined the signal build-up process to study the carriers' accumulating process for SE and ASE. The feedback information showed that the charge carriers' band-filling process could be completed within several picoseconds, and that this process was independent of the sizes of  $\text{MAPbBr}_3$  emitters.<sup>33</sup> Though the charge carriers' density of ASE far exceeded that of SE, the band-filling process of these two PL processes were nearly identical. That is, different from other

illuminant materials, the ASE of  $\text{CH}_3\text{NH}_3\text{PbBr}_3$  cubic emitters did not take much more time to complete charge carriers' accumulation compared with that of SE. This relatively faster ASE build-up may render itself more competitive for lasing applications.

## Conclusions

In this paper, we presented the 1P- and 2P-pumped size-dependent optical properties of  $\text{CH}_3\text{NH}_3\text{PbBr}_3$  perovskite cubic microcrystals by steady-state and time-resolved experiments. The 1P-pumped results showed that size had a very important role in modulating the SE and ASE characteristics from three aspects: emission position, threshold value, and fluorescence lifetimes. First, the SE and ASE were all linearly red-shifted to longer wavelengths with increasing crystal sizes. Second, the larger-sized  $\text{CH}_3\text{NH}_3\text{PbBr}_3$  cubic crystals showed relatively lower threshold values, and this phenomenon could be ascribed to their stronger light-absorption intensity. Third, time-resolved PL dynamics results showed that larger-sized  $\text{CH}_3\text{NH}_3\text{PbBr}_3$  perovskite cubic microcrystals had a faster lifetime ASE with higher purity. Finally, compared with 1P excitation, the 2P-pumped ASE  $P_{\text{th}}$  was reduced by nearly one order of magnitude due to a sharply increased line gain length. We believe that the 2P effect will open another avenue for fluorescence studies, and may be the ideal solution for overcoming some problems precluding the development of perovskite-based illuminated applications. Also, this work may focus more attention on large-size perovskite cubic crystals, and may make the cubic pattern the next paradigm to realize satisfactory perovskite-based luminescence applications.

## Acknowledgements

This work was supported by the National Natural Science Foundation of China and National 973 program under grants #21473076, #21473077, #21603083, #61590930, #2014CB921302, #21273096, and also by Doctoral Fund Ministry of Education of China (20130061110048).

## References

- 1 J. H. Im, I. H. Jang, N. Pellet, M. Grätzel and N. G. Park, *Nat. Nanotechnol.*, 2014, **9**, 927–932.
- 2 Q.-F. Dong, Y.-J. Fang, Y.-C. Shao, P. Mulligan, J. Qiu, L. Cao and J.-S. Huang, *Science*, 2015, **347**, 967–970.
- 3 T. S. Kao, Y.-H. Chou, C.-H. Chou, F.-C. Chen and T.-C. Lu, *Appl. Phys. Lett.*, 2014, **105**, 231108.
- 4 Y. Wang, X.-M. Li, J.-Z. Song, L. Xiao, H.-B. Zeng and H.-D. Sun, *Adv. Mater.*, 2015, **27**, 7101–7108.
- 5 F. Zhang, H.-Z. Zhong, C. Chen, X.-G. Wu, X.-M. Hu, H.-L. Huang, J.-B. Han, B.-S. Zou and Y.-P. Dong, *ACS Nano*, 2015, **9**, 4533–4542.
- 6 G.-C. Xing, N. Mathews, S. S. Lim, N. Yantara, X.-F. Liu, D. Sabba, M. Grätzel, S. Mhaisalkar and T. C. Sum, *Nat. Mater.*, 2014, **13**, 476–480.
- 7 Z.-Y. Zhang, H.-Y. Wang, Y.-X. Zhang, Y.-W. Hao, C. Sun, Y. Zhang, B.-R. Gao, Q.-D. Chen and H.-B. Sun, *Sci. Rep.*, 2014, **6**, 27286.
- 8 Y.-S. Park, S.-J. Guo, N. S. Makarov and V. I. Klimov, *ACS Nano*, 2015, **9**, 10386–10393.
- 9 H.-M. Zhu, Y.-P. Fu, F. Meng, X.-X. Wu, Z.-Z. Gong, Q. Ding, M. V. Gustafsson, M. T. Trinh, S. Jin and X.-Y. Zhu, *Nat. Mater.*, 2015, **14**, 636–643.
- 10 R. Dhanker, A. N. Brigeman, A. V. Larsen, R. J. Stewart, J. B. Asbury and N. C. Giebink, *Appl. Phys. Lett.*, 2014, **105**, 151112.
- 11 C. Wehrenfennig, M. Z. Liu, H. J. Snaith, M. B. Johnston and L. M. Herz, *J. Phys. Chem. Lett.*, 2014, **5**, 1300–1306.
- 12 S. G. R. Bade, J. Q. Li, X. Shan, Y.-C. Ling, Y. Tian, T. Dilbeck, T. Besara, T. Geske, H.-W. Gao, B.-W. Ma, K. Hanson, T. Siegrist, C.-Y. Xu and Z.-B. Yu, *ACS Nano*, 2016, **10**, 1795–1801.
- 13 Y.-Q. Xu, Q. Chen, C.-F. Zhang, R. Wang, H. Wu, X.-Y. Zhang, G.-C. Xing, W. W. Yu, X.-Y. Wang, Y. Zhang and M. Xiao, *J. Am. Chem. Soc.*, 2016, **138**, 3761–3768.
- 14 B. R. Sutherland, S. Hoogland, M. M. Adachi, C. T. O. Wong and E. H. Sargent, *ACS Nano*, 2014, **10**, 10947–10952.
- 15 Y. Yamada, T. Nakamura, M. Endo, A. Wakamiya and Y. Kanemitsu, *J. Am. Chem. Soc.*, 2014, **136**, 11610–11613.
- 16 S. D. Stranks, V. M. Burlakov, T. Leijtens, J. M. Ball, A. Goriely and H. J. Snaith, *Phys. Rev. Appl.*, 2014, **2**, 034007.
- 17 D. Shi, V. Adinolfi, R. Comin, M.-J. Yuan, E. Alarousu, A. Buin, Y. Chen, S. Hoogland, A. Rothenberger, K. Katsiev, Y. Losovyj, X. Zhang, P. A. Dowben, O. F. Mohammed, E. H. Sargent and O. M. Bakr, *Science*, 2015, **347**, 519–522.
- 18 Y.-J. Fang, Q.-F. Dong, Y.-C. Shao, Y.-B. Yuan and J.-S. Huang, *Nat. Photonics*, 2015, **9**, 679–686.
- 19 S. Yakunin, L. Protesescu, F. Krieg, M. I. Bodnarchuk, G. Nedelcu, M. Humer, G. De Luca, M. Fiebig, W. Heiss and M. V. Kovalenko, *Nat. Commun.*, 2015, **6**, 8056.
- 20 V. D'Innocenzo, A. R. S. Kandada, M. De Bastiani, M. Gandini and A. Petrozza, *J. Am. Chem. Soc.*, 2014, **136**, 17730–17733.
- 21 Q. Zhang, S. T. Ha, X. F. Liu, T. C. Sum and Q. H. Xiong, *Nano Lett.*, 2014, **10**, 5995–6001.
- 22 J. Xing, X. F. Liu, Q. Zhang, S. T. Ha, Y. W. Yuan, C. Shen, T. C. Sum and Q. H. Xiong, *Nano Lett.*, 2015, **7**, 4571–4577.
- 23 A. S. Bar-Noam, N. Farah and S. Shoham, *Light: Sci. Appl.*, 2016, **5**, e16007.
- 24 K. Obata, A. El-Tamer, L. Koch, U. Hinze and B. N. Chichkov, *Light: Sci. Appl.*, 2013, **2**, e116.
- 25 W. Xiong, Y.-S. Zhou, X.-N. He, Y. Gao, M. Mahjouri-Samani, L. Jiang, T. Baldacchini and Y.-F. Lu, *Light: Sci. Appl.*, 2012, **1**, e6.
- 26 J. Pan, S. P. Sarmah, B. Murali, I. Dursun, W. Peng, M. R. Parida, J.-K. Liu, L. Sinatra, N. Alyami, C. Zhao, E. Alarousu, T. K. Ng, B. S. Ooi, O. M. Bakr and O. F. Mohammed, *J. Phys. Chem. Lett.*, 2015, **6**, 5027–5033.
- 27 Y. Yamada, T. Yamada, L. Q. Phuong, N. Maruyama, H. Nishimura, A. Wakamiya, Y. Murata and Y. Kanemitsu, *J. Am. Chem. Soc.*, 2015, **137**, 10456–10459.

- 28 T. Yamada, Y. Yamada, H. Nishimura, Y. Nakaike, A. Wakamiya, Y. Murata and Y. Kanemitsu, *Adv. Energy Mater.*, 2016, **2**, 1500290.
- 29 V. D'Innocenzo, A. R. S. Kandada, M. De Bastiani, M. Gandini and A. Petrozza, *J. Am. Chem. Soc.*, 2014, **136**, 17730–17733.
- 30 J. H. Heo, D. H. Song and S. H. Im, *Adv. Mater.*, 2014, **26**, 8179–8183.
- 31 Z. Y. Zhang, X. Chen, H. Y. Wang, M. Xu, B. R. Gao, Q. D. Chen and H. B. Sun, *Phys. Chem. Chem. Phys.*, 2015, **44**, 30084–30089.
- 32 B. R. Sutherland and E. H. Sargent, *Nat. Photonics*, 2016, **10**, 295–302.
- 33 J. S. Manser and P. V. Kamat, *Nat. Photonics*, 2014, **8**, 737–743.